

Chapter 11

Towards In-Flight Measurements of Helicopter Blade Tip Vortices

Kolja Kindler, Karen Mulleners and Markus Raffel

Abstract In the framework of the AIM project the near field of the blade tip vortex of a full-scale helicopter in simulated hover flight was investigated by combining three-component Particle Image Velocimetry and Background Oriented Schlieren measurements. The velocity field measurements in the range of wake ages of $\psi_v = 1^\circ$ to 30° in azimuth provided a reference for a quantitative analysis of the Schlieren results yielding vortex core density estimates. Ongoing vortex roll-up was observed at $\psi_v = 1^\circ$ while considerable aperiodicity was persistent thereafter. The vortex parameters for $\psi_v > 1^\circ$ were consistent with the Scully vortex model. The particular challenges of full-scale, outdoor testing, especially the limited spatial resolution and aperiodicity effects, resulted in elevated measurement uncertainty as compared to sub-scale experiments.

11.1 Introduction

Blade tip vortices trailing from the main rotor of a helicopter are the dominant coherent structures of the rotor wake, especially, with respect to fluid-structure interaction, aeroacoustics, etc. As such, the blade tip vortex has drawn considerable attention in terms of analytical, experimental, and increasingly numerical investigations [1].

Due to the inherent complexity of the helicopter flow field, wind tunnel experiments as well as numerical investigations by means of computational fluid dynamics

K. Kindler (✉)

German Aerospace Center, Linder Höhe, 51147 Köln, Germany
e-mail: kolja.kindler@dlr.de

M.Mulleners · M. Raffel

German Aerospace Center (DLR), Bunsenstr. 10, 37073 Göttingen, Germany

M.Mulleners

Institute for Turbo Machinery and Fluid Dynamics, University of Hannover, Appelstr. 9,
D-30167 Hannover, Germany

(CFD) are rather intricate, time-consuming, and cost-intensive [2]. Furthermore, the relevant dimensionless parameters, e.g. the reduced vortex Reynolds numbers $Re = \Gamma_v / \nu$ (with the circulation Γ_v and the kinematic viscosity ν), obtained in sub-scale experiments are often not in accordance with the full-scale quantities. Hence, characteristic aerodynamic scaling is exacerbated.

Therefore, it is appealing to adapt and implement available experimental methods to probe the blade tip vortex characteristics *in situ*, i.e. in flight. Full-scale, in-flight experiments provide access to a much larger range of flight parameters than typically attainable in wind tunnel testing. Complex aerodynamic problems such as blade-vortex interaction and tip vortex control can be addressed directly. To this end, the near field of the tip vortex¹ is of particular importance since measures of active and passive vortex control target this crucial stage of development. Despite its significance, only few experimental reports addressing full-scale blade tip vortices [3–5] consider the near field.

Hitherto, most of the sub-scale experiments utilised Laser Doppler Velocimetry (LDV) (e.g. [6, 7]). Although providing a high measurement accuracy at large sampling rates, LDV requires an independent determination of the vortex centre position in relation to the measurement volume. Thus, it is inadequate for in-flight testing. Particle Image Velocimetry (PIV) on the other hand, captures an entire region around the vortex providing areal swirl velocity information and instantaneous vortex centre position derived from it (see e.g. [8] and references therein). However, the application of PIV, as well as LDV, for ground independent testing would require cumbersome instrumentation to be integrated into the helicopter.

A promising technique for in-flight velocity field investigations is Light Detection and Ranging (LIDAR) which is reported in Chap. 12. While the technical implementation of a LIDAR system in a helicopter is reasonably practicable, the supply of tracer particles in the measurement area is rather challenging.

Aside LIDAR, Background Oriented Schlieren (BOS) appears to be the most practical method for efficient full-scale in-flight helicopter investigations. The BOS technique is based on visualising light deflections caused by density gradients within the flow field. In order to quantify these deflections artificial speckle patterns are imaged with and without an aerodynamic structure influencing the light path. The vortex structure is subsequently reconstructed by cross-correlating image-reference pairs [9, 10]. BOS is particularly suitable for ground independent testing because natural formations such as grass, cornfields, and skirts of forests provide adequate backgrounds [11–13]. In the framework of the AIM project a BOS sensor unit was developed and certified which integrates a digital high-resolution camera capable of rotor synchronised image acquisition into the helicopter.

The present investigation includes BOS measurements of the near field of the blade tip vortices. Beyond qualitative vortex visualisation, quantitative density field information can be derived from the monoscopic BOS data if rotational symmetry of the vortical structures can be presumed [12, 14, 15]. However, rotational symmetry

¹ The near field denotes the region directly behind the blade tip where the initial development of tip vortex takes place.

of the blade tip vortex within the near field cannot be expected a priori. Therefore, a reference measurement of the vortex velocity field in simulated hover flight, i.e. with the helicopter fixed on the ground, was carried out by means of PIV. Based on three-component PIV data at vortex ages of $\psi_v = 1^\circ$ to 30° deviations from rotational symmetry within the vortex formation stage were evaluated and constraints for the BOS results were defined. This investigation was intended to lay the foundations for future ground-independent, in-flight measurements including tip vortex visualisation and to provide quantitative core density estimations.

11.2 Experimental Methods

11.2.1 Test Helicopter

For this study DLR's MBB Bo105 experimental helicopter (see Fig. 11.1) was fixed on the ground and operated in simulated hover flight (in ground effect). The fixation of the helicopter is experimentally most favourable and the development of tip vortices within the range of wake ages relevant to this study can be anticipated to be well defined. The main rotor of the test helicopter had $N_b = 4$ hingeless blades of rectangular planform with a radius of $R = 4.91$ m, a chord length of $c = 0.27$ m, a solidity of $\sigma = N_b c / (\pi R) = 0.07$, and -8° linear blade twist. The angular velocity of the main rotor was $\Omega = 44$ rad/s yielding a blade tip Mach number of $Ma = 0.64$. During simulated hover flight, the helicopter generated approximately $T = 20000$ N thrust, corresponding to a thrust coefficient of $C_T = T / (\rho \pi \Omega^2 R^4) = 0.0046$ resulting in a blade loading of $C_T / \sigma \simeq 0.066$.

11.2.2 Particle Image Velocimetry

Measurement configuration. The measurement plane was located on the port-side, parallel to the trailing edge of the blade (Fig. 11.2). The PIV data acquisition system



Fig. 11.1 DLR's MBB Bo105 test helicopter

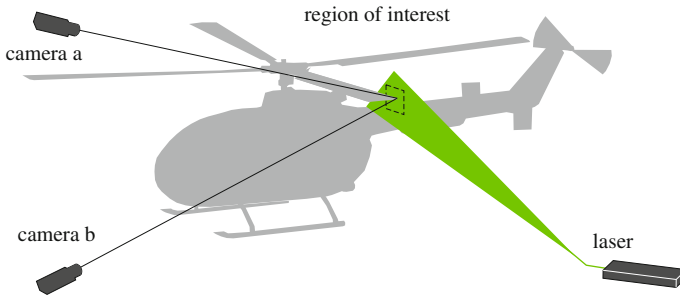


Fig. 11.2 Experimental set-up for stereoscopic PIV measurements of the blade tip vortex

consisted of two 10.7 Mpx CCD cameras equipped with 300 mm objectives in a stereoscopic configuration. The cameras were positioned on a vertical support ca. 1.5 m above and 2.1 m below the rotor plane in idle condition at a distance of 10 m away from the observation area. Illumination of the flow field was provided by means of a laser light sheet fed by a double cavity Nd:YAG pulse laser with a wavelength of 532 nm and an energy of 280 mJ per pulse. The laser sheet was oriented parallel to the trailing edge of the blade such that the tip vortices are likely to be measured in a plane normal to their axis. The spatial resolution of the image acquisition system was 4 px/mm (corresponding to 1080 px/c) for a field of view (FOV) of approximately 0.9×0.6 m. The PIV system was synchronised with the main rotor taking advantage of an inductive rotor position indicator permanently installed for rotor balancing purposes.

When it comes to on-board in-flight PIV applications, the provision of a homogeneous and sufficiently dense tracer particle distribution is an extremely demanding task. The atmospheric background conditions, i.e. even moderate cross-winds, might strongly alter the optimal injection point and, therefore, the tracer density within the field of view. The tracer generation and supply including an injection nozzle reaching approximately 3 m above the rotor disk, were realised on a mobile platform which could be relocated in response to the outer conditions at a distance of one rotor radius apart from the rotor disk. During the tests, the ambient conditions were close to the international standard atmosphere at an average temperature and atmospheric pressure of 10 °C and 1.015 hPa, respectively, with calm winds below 1.5 m/s and intermittent gusts of less than 4 m/s.

Data evaluation methodology. The stereoscopic PIV data were evaluated according to standard procedures [16]. The intensity images acquired were high-pass filtered and normalised using the series minimum greylevel image prior to further processing. A camera view misalignment correction was computed for each time series as part of the image de-warping to compensate for small image offsets which would be greatly amplified due to the large scale geometry of the set-up [17].

To optimise the interrogation window size and overlap, the scheme of Richard and van der Wall [18] was followed. The interrogation window size was minimised with respect to an acceptable signal-to-noise ratio while the window overlap was

maximised to avoid artificial smoothing of velocity gradients. The correlation analysis of the interrogation windows represents a low-pass filter, limiting the peak velocities accessible [18]. By increasing the sampling window overlap, the probability of an interrogation window being perfectly centred at the maximum velocity increases, minimising spatial averaging effects by the interrogation window itself. In this case, rectangular cross-correlation windows of width 32 px with an overlap of approximately 94 % were used. The corresponding physical resolution, the ratio of the PIV measurement volume to chord length, is $L_m/c = 0.0296$ which translates into $L_m/r_c = 0.593$ using $r_c = 0.05c$ as an estimate of the vortex core radius. This value is at the lower range of numerous recent investigations ranging from $L_m/r_c = 0.19$ to 2.6 (cf. [19] and references therein) but is at least a factor of 3 coarser than the commonly accepted resolution requirement of $L_m/r_c < 0.2$ [20]. However, the actual resolution depends on vortex age. Additionally, a multi-grid evaluation scheme is used within the correlation analysis, in order to increase the resolution of regions of strong shear.

Prior to further analysis, the averaged background velocities within the observation area were subtracted from the instantaneous velocity fields, which mainly affected the out-of-plane component and does not interfere with the vortex centre identification. Subsequently, the vortex centres were identified using the scalar function introduced by Graftieaux et al. [21] (in its discrete form)

$$\Gamma_1(P) = \frac{1}{N} \sum_S \frac{(PM \times U_M) \hat{e}_x}{\|PM\| \cdot \|U_M\|} \quad (11.1)$$

where N is the number of points in the two-dimensional neighbourhood S of any given point P in the y, z plane, M lies in S , \hat{e}_x is the unit vector in x direction, and U_M is the in-plane velocity at M . The extremum of Γ_1 is identified with the vortex centre.² Unlike alternative criteria for vortex centre identification such as vorticity peak detection, λ_2 , etc., the Γ_1 function does not require velocity field derivatives or the out-of-plane component reconstructed during evaluation and, therefore, is less susceptible to experimental noise (for a comprehensive review of the robustness of a variety of gradient-based operators and velocity field as well as convolution based methods it should be referred to [19, 22]). Especially, large-scale PIV measurements of unsteady flow fields tend to yield spiky velocity derivatives leading to less reliable vortex centre identification than the scheme based on Eq. 11.1.

Finally, the inclination of the vortex axis with respect to y and z spanning the measurement plane were estimated based on the out-of-plane velocity gradients ($\partial u/\partial y$, $\partial u/\partial z$) outside two times the core radius and the ratio of maximum swirl and core radius $V_{s,max}/r_c$ using an iterative procedure [19]. The inclination angles were found to be smaller than 3.5° for the data relevant to this study, which is considered negligible, rendering a transformation into the vortex system unnecessary.

Measurement accuracy assessment. The data quality of the full-scale PIV measurements is found to vary strongly for subsequent time steps. The measurement

² Note that Γ_1 is not to be confused with Γ_v the circulation of a vortex.

noise level is considerably higher than typically achieved in laboratory experiments. Obviously, these variations are primarily due to the varying or intermittently inhomogeneous tracer concentration including tracer density gradients within the region of interest. Due to the unsteady nature of the flow field dissociated tracer patches of variable size are commonly found. Because the tracers are injected from above the rotor plane, the downwash tends to induce higher tracer concentrations inboard of the blade tip, while the fluid from the recirculation region outboards features stronger patchiness and, on average, lower tracer concentration.

The image pairs where the lack of tracers resulted in non-physically dysmorphic or undetectable vortex structures in the velocity fields were excluded from the analysis. As a result, approximately 10 % of the series of 120 velocity fields at each wake age were discarded. The local tracer density represented the intrinsic limit of measurement resolution and accuracy as it defines the minimal interrogation window size and the validity of the results.

11.2.3 Background Oriented Schlieren

The BOS sensor unit. The sensor unit for the initial measurements consisted of two high-resolution Canon OES 1Ds Mark II cameras with a focal length of $f = 70$ to 200 mm mounted on an optical rail placed inside the helicopter (Fig. 11.3a). Images were acquired at $f = 200$ mm, corresponding to an f-number of $f_{\#} = f/22$ at a resolution of 0.169 mm/px.

Based on the lessons learned from the initial measurements, an advanced in-flight BOS sensor unit was developed, manufactured and certified (Fig. 11.3b). The sensor consisted of the same camera and lens as above cased in an aluminium box which is

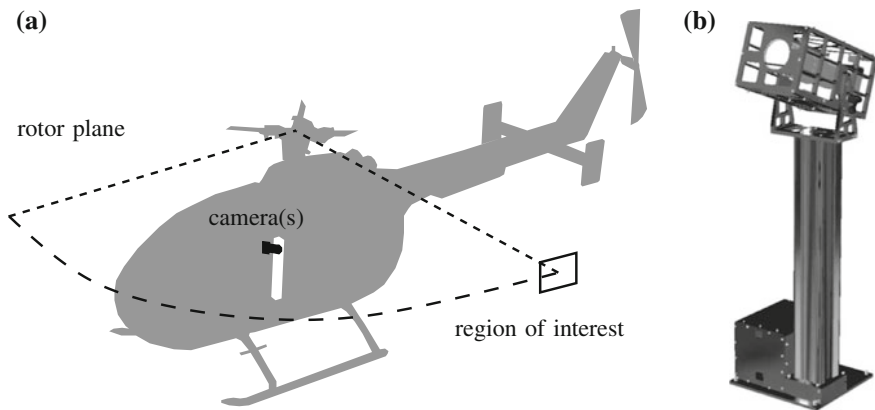


Fig. 11.3 Sketch of the airborne stereoscopic BOS imaging system as used for preliminary investigations (a); the sensor unit designed and certified for rotor-synchronised in-flight measurements (b)

pivotable in the vertical. The box was supported by a standard optical rail mounted on an available base plate behind the co-pilot’s seat of the helicopter. Additionally, the construction featured a second casing for trigger electronics and power supply. The acquisition of image series at constant frame rate was initiated by a trigger signal synchronised with the main rotor. The camera was remotely controlled by a portable computer which did not have to be included in the certification process.

Measurement configuration. The background was provided by an artificial vari-coloured speckle pattern of 4×4 m in size attached to the front of a hangar approximately 5 m above ground. The distance between the camera and the expected tip vortex position was approximately R , while the distance to the background was $5R$. The sampling frequency was 4 Hz yielding a sufficient inter-framing time for the vortex to be shifted to an initially undisturbed area of the image. The image displacement, δz , measured using an artificial background at a distance of $1.5R$ from the vortex showed a symmetrical structure (Fig. 11.4). The interrogation window size was 36×36 px with a 50 % window overlap and the global uncertainty, in this case, was less than 10 % of the deflections. Atmospheric conditions close to the standard atmosphere at 24°C were considered.

Schlieren measurement accuracy. Since the deviations of the apparent pixel shift, δz , are mainly of random nature uncertainties can be expected cancel during subsequent integration. The systematic error of the deviation angle, $\Delta\gamma$, was due to uncertainties of the magnification, m , and the distance between the vortex core and background, a and is given by

$$\Delta\gamma = \left| -\frac{\delta z}{m^2 a} \Delta m \right| + \left| -\frac{\delta z}{m a^2} \Delta a \right|. \tag{11.2}$$

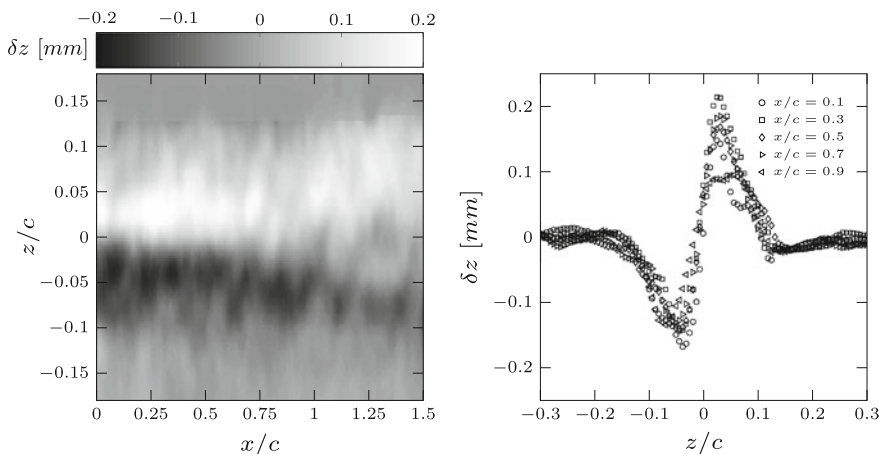


Fig. 11.4 Image displacement δz and displacement profiles extracted at $x/c = 0.1, 0.2, 0.5, 0.7$ and 0.9 ($\psi_v = 0.3^\circ, 0.6^\circ, 1.6^\circ, 2.2^\circ$ and 2.8°) downstream from the trailing edge of the blade

These errors caused a constant deviation of γ which translates into a constant deviation of the tomographic reconstruction. The density uncertainties specified below were estimated based on the relative errors of γ .

11.3 Results and Discussion

11.3.1 Average Vortex Velocity Fields

With the exception of vortex ages of $\psi_v < 5^\circ$, the conditionally averaged velocity and the corresponding vorticity fields of the blade tip vortex indicated a spherical cross-section while the z-component, i.e. the cross-flow component, exhibits noticeable stretching in y direction (Fig. 11.5). This departure from circularity is associated with the minor inclination of the vortex axes with respect to the measurement plane. The extension of the cross-flow field to the lower left represents the drag bucket behind the rotor blade. Due to the blade circulation exhibiting a strong gradient towards the tip, a sheet of trailed vorticity is shed into the wake, which is recognisable in the vorticity distribution from the vortex centre down to the left of the image.

11.3.2 Vortex Formation Stage

In order to trace effects of vortex formation, i.e. shear layer roll-up, the rotational symmetry of the vortex velocity fields was considered. Approximating Γ_1 by a bivariate Cauchy distribution of the form

$$L = \frac{a}{1 + \frac{x^2}{b} + \frac{y^2}{c}}, \quad (11.3)$$

where a, b and c are fit parameters, the principle axes were derived and the vortex circularity was expressed as the principal axes ratio

$$\epsilon = \sqrt{1 - \frac{b}{c}}. \quad (11.4)$$

Additionally, the inclination angle of the major axis with respect to the horizontal was extracted.

The distribution of the axis ratio indicated noticeable asymmetry of the vortices which decreased with increasing wake age (Fig. 11.6a). At the same time, the inclination angles β were uniformly distributed irrespective of $\psi_v = 1^\circ$ (Fig. 11.6b). For the youngest wake age considered, the major axis had a preferential orientation with respect to the horizontal which was associated with the predominantly spiral

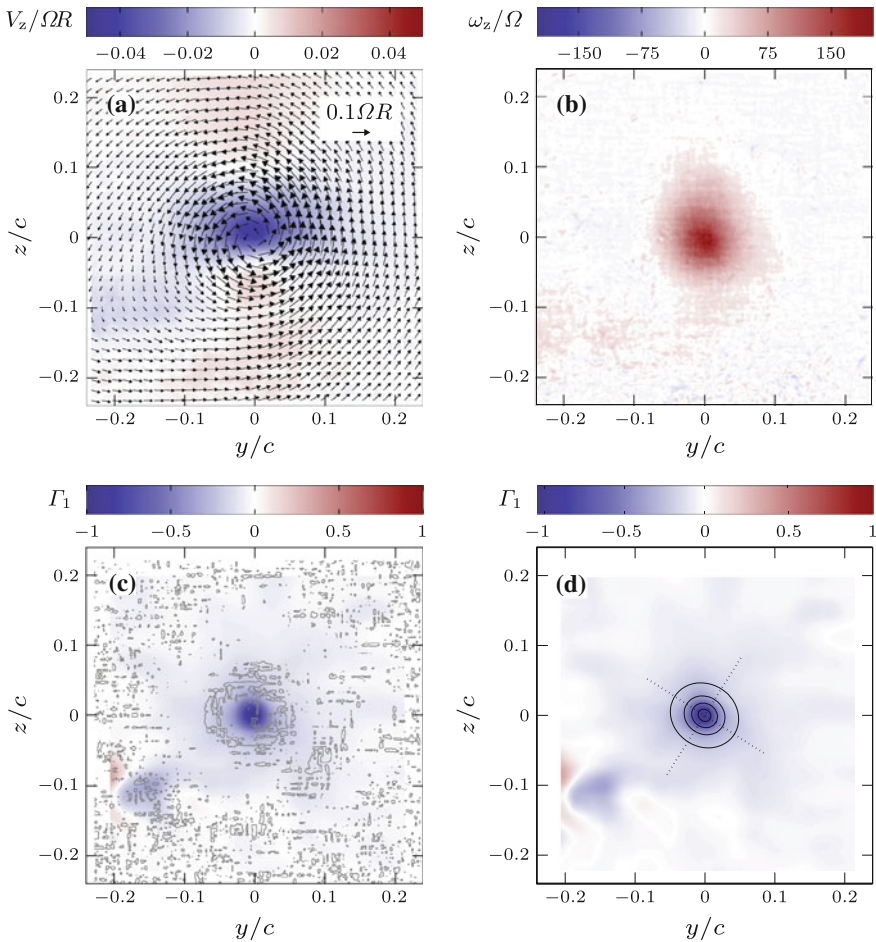


Fig. 11.5 The conditionally averaged velocity field $\psi_v = 5^\circ$ (a) and the corresponding in-plane vorticity component ω_x (b). A comparison of Γ_1 with the zero-crossing of λ_2 (c) and the circularity of the vortex cross-section derived from Γ_1 for a representative instantaneous field at $\psi_v = 5^\circ$ (d). Velocities are scaled by the blade tip speed ΩR , the in-plane component of vorticity scaled by the angular velocity of the main rotor, Ω

structure in this range of development. Downstream from the initial vortex formation stage, noticeable aperiodicity of the vortex velocity fields indicated incomplete relaxation of the cores. In the range of wake ages considered, aperiodicity effects imposed the major constraint to axial symmetry which contributed to the elevated level of uncertainty of the velocity vortex profiles [23].

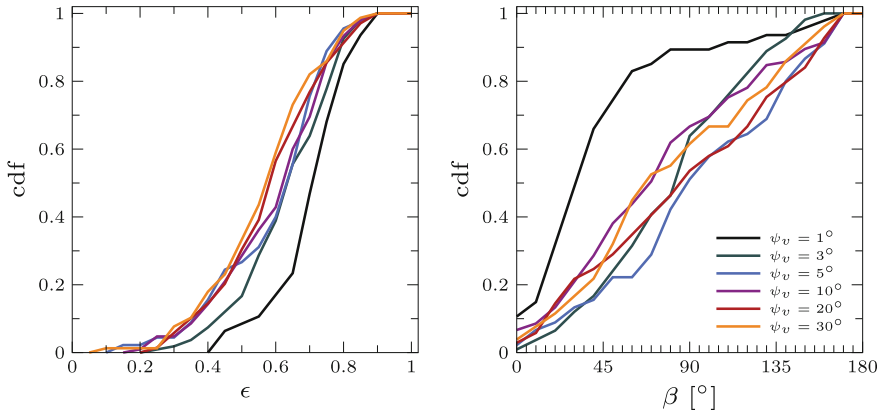


Fig. 11.6 Cumulative probability density of the principal axis ratio ϵ and the inclination angle of the major axis β

11.3.3 Low-Order Vortex Approximation

In order to facilitate a mutual comparison of the BOS and PIV results, the velocity fields were approximated by a low-order vortex velocity model [24], which is outlined below for convenience. The non-dimensional tangential, radial, and axial velocity take the form

$$\bar{V}_\Theta = \frac{\bar{r}}{(1 + \bar{r}^{2n})^{1/n}}, \quad (11.5)$$

$$\bar{V}_r = -\frac{2(1+n)\bar{r}^{2n-1}}{1 + \bar{r}^{2n}}, \quad (11.6)$$

$$\bar{V}_x = \frac{4n(1+n)\bar{r}^{2(n-1)}}{(1 + \bar{r}^{2n})^2} \bar{x}, \quad (11.7)$$

where $\bar{V}_\Theta = V_\Theta/V_{\Theta,0}$ with $V_{\Theta,0} = \Gamma_v/2\pi r_c$, $\bar{r} = r/r_c$, $\bar{V}_r = V_r r_c/\nu$, $\bar{V}_x = V_x r_c/\nu$, and $\bar{x} = x/r_c$. Γ_v is the circulation of the vortex, ν is the dynamic viscosity of air. The core radii r_c and $V_{\Theta,0}$ were determined by least-square fitting. Treating n initially as free parameter to be identified, yielded values very close to $n = 1$, corresponding to the Scully vortex model. Hence, this model was applied in the remainder of the evaluation, reducing the degrees of freedom of the parameter identification to Γ_v , r_c , and \bar{x} .

The tangential, radial, and axial velocity profiles were azimuthally averaged with respect to the vortex axis prior to conditionally averaging the time series which were then approximated by the model (Fig. 11.7). Both the tangential and axial velocity, V_Θ and V_x , are consistent with the model of Eqs. 11.5 and 11.7, where the standard deviation is below 0.03 ΩR . The weak radial velocity component V_r (not shown)

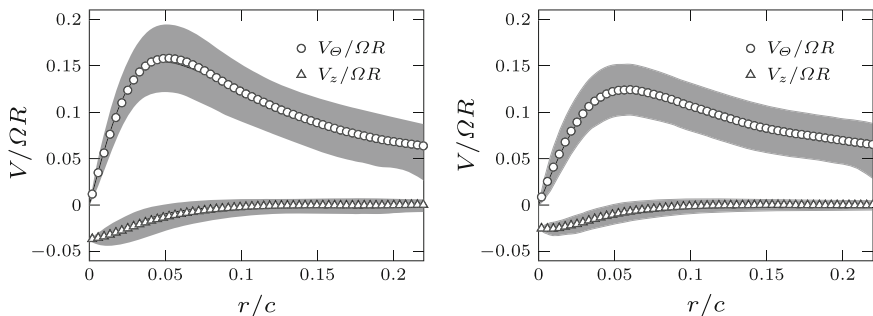


Fig. 11.7 Velocity profiles of blade tip vortex at $\psi = 3^\circ$ (left) and $\psi = 30^\circ$ (right); the shading denotes the standard deviation of the measured data, lines represent the best fit to Eqs. 11.5 and 11.7 using $n = 1$ (Scully vortex)

is found to vanish to within the measurement accuracy. The radial component is particularly sensitive to effects of lateral vortex convection and background effects. Additionally, the downwash contributes to depressing the radial velocities inboard of the tip affecting the axial average of the velocity profiles. This is especially the case for a hovering rotor, where at the inboard side of the vortex a strong mean downwash is superimposed on the vortex velocity field while at the outboard side no such downwash is present. In forward flight, the mean downwash is significantly smaller and this effect would be largely alleviated.

The average vortex core radii for $\psi \geq 3^\circ$ were in the range $\bar{r} = 0.04$ to 0.06 with peak tangential velocities of $\bar{V}_\Theta = 0.15$ to 0.12 . In absence of any reference near field data these results cannot be validated. However, earlier full-scale measurements resulted in peak swirl velocities of $\bar{V}_\Theta = 0.2$ to 0.5 and initial core radii of $\bar{r} = 0.02$ to 0.03 in the far field. This is in agreement with recent sub-scale measurements [18] although Re_v is only half as large. The reasons for this difference are manifold. First, the persistent residual asymmetry indicates that the vortex roll-up is incomplete within the wake age interval investigated. In this area the initial core size is related to the boundary layer thickness close to blade tip, which in turn depends on the tip Mach number, angle of attack, etc.. The deviations from rotational symmetry were translated into reduced tangential velocities and increased core radii by the averaging procedure applied. Furthermore, straining effects which promote concentration of the core are known to take effect at larger wake ages. The overall increased measurement noise level caused additional smoothing of the steep velocity gradients.

11.3.4 Vortex Core Densities

The vortex core density fields were reconstructed from the Schlieren results using a method based on an inverse Radon transform according to [12] (Fig. 11.8).

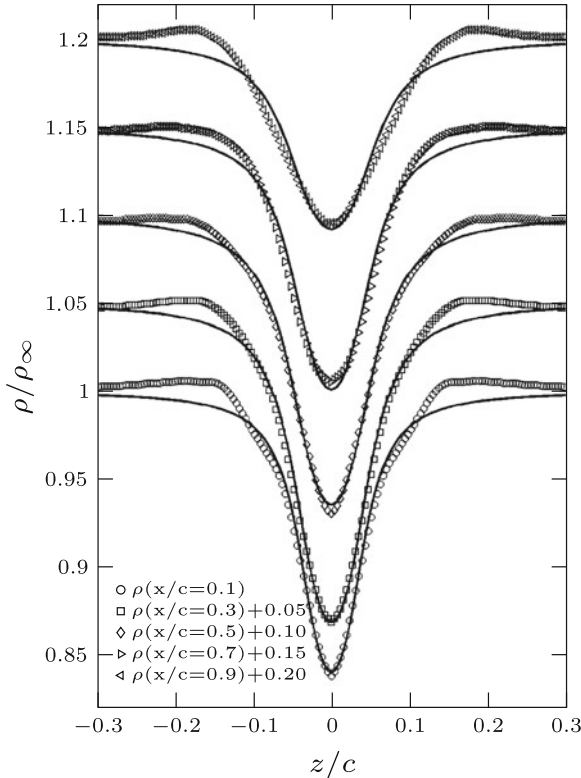


Fig. 11.8 Tomographic reconstruction of the density profiles at $x/c = 0.1, 0.3, 0.5, 0.7,$ and 0.9 ($\psi_v = 0.3^\circ, 0.6^\circ, 1.6^\circ, 2.2^\circ,$ and 2.8°). The *solid lines* represent the best fit of Eq. 11.8

Subsequently, the azimuthally averaged density profiles, were approximated by the Scully vortex model (Eq. 11.5–11.7). Additionally, the reduced density reads [25]:

$$\frac{\rho}{\rho_\infty} = \left(1 - \frac{\kappa - 1}{1 + (r/r_c)^2} \zeta \right)^{\frac{1}{1-\kappa}}, \quad (11.8)$$

assuming inviscid and isentropic flow. Here, κ is the specific heat ratio and ζ is a fit-parameter together with r_c . The considerations were restricted to an area between $x/c = 0$ to 1 , i.e. $\psi = 0$ to 3° where effects of vortex motion towards the fuselage were expected to be negligible.

The total density loss was approximately 25 % at $x/c = 0.1$ and decreased towards 10 % at $x/c = 0.9$. The best fit of Eq. 11.8 yielded $\bar{r} = 0.043, 0.049, 0.055, 0.054,$ and 0.060 at $x/c = 0.1, 0.3, 0.5, 0.7,$ and 0.9 . Due to the helicopter motion during the measurement, the relative uncertainty of the density data did not fall below 20 % which translated into an estimated core radius deviation of $\Delta r_c = 0.005$ without

taking into account resolution effects. The reduced density exceeded $\rho / \rho_\infty = 1$ at the core boundaries and relaxed radially. Although this behaviour is not included in the Scully model (Eq. 11.8) the fits were in satisfactory agreement with the measurements.

The averaged vortex radii determined from the three-component PIV measurements were found to be in agreement with the corresponding values derived from BOS measurements of the same experimental configuration as reported in [12]. At a wake age of $\psi_v = 3^\circ$ PIV and BOS yield a core radius of $\bar{r} = 0.055$ and 0.060 , respectively, at a core density drop of 10% with respect to the ambient and a peak tangential velocity of $\bar{V}_\Theta / \Omega R = 0.149$. It should be noted that at this particular vortex age the roll-up process was incomplete. The conformity of the full-scale PIV and BOS results can partly be ascribed to the fact that both correlation based optical methods share similar limitations in terms of spatial resolution. However, the two independent experiments provide sufficient cross-validation to within the measurement accuracy.

11.4 Conclusions

An airborne rotor synchronised BOS image acquisition system was developed and certified to study the tip vortex characteristics in situ under various flight conditions. First BOS results in the near field yielded quantitative core density estimations, where rotational symmetry was assumed. To quantify effects of vortex formation in the near-field, three-component velocity measurements on a full-scale Bo105 helicopter in ground effect were performed as a reference measurement. The analysis of the range of wake ages of $\psi_v = 1^\circ$ to 30° indicated sufficient rotational symmetry to be attained closely downstream from the blade tip. Within the near-field, i.e. the vortex formation region, the measurement uncertainty was elevated. Due to persistent aperiodicity of the vortex flow field, the peak swirl velocities were underestimated while core radii were overestimated. Thereafter, the average tangential and axial velocities were well described by the Scully vortex model. The vortex core radii derived from velocity and Schlieren measurements coincide to within measurement uncertainty.

Based on the results presented here a straightforward integration of an available measurement techniques such as BOS can be efficiently utilised for in-flight testing. Thereby, the range of accessible flight parameters can be expanded when compared to wind tunnel testing. Future efforts will include experiments probing the tip vortex trajectories in the far field as well as investigations of different measures of vortex control and their impact on the near and far field. Finally, blade-vortex interaction will be addressed within the full-scale system.

Acknowledgments The analysis was performed in the framework of the US/German Memorandum of Understanding on Helicopter Aerodynamics, Task VIII “Rotor Wake Measurement Techniques”. The authors are greatly indebted to F. Leopold from the French-German Research Institute of Saint-Louis and E. Goldhahn from the Institute for Turbo Machinery, University of Hannover for their

valuable contributions to the realisation and analysis the Schlieren measurements. Furthermore, the dedicated support by the helicopter crew R. Gebhard and U. Göhmann as well as by our colleagues B. G. van der Wall, H. Richard, M. Jönsson, and M. Kühn is gratefully acknowledged.

References

1. A.T. Conlisk, Modern helicopter rotor aerodynamics. *Progr. Aerospace Sci.* **37**, 419 (2001)
2. J.W. Lim, T.A. Nygaard, R. Strawn, M. Potsdam, BVI airloads prediction using CFD/CSD loose coupling, in *4th AHS Vertical Lift Aircraft Design Conference*, San Francisco, CA, USA, 16–20 Jan 2006
3. H. Richard, M. Raffel, Rotor wake measurements: full-scale and model tests, in *58th Annual Forum of the American Helicopter Society*, Montreal, Canada, 11–13 June 2002
4. C.V. Cook, The structure of the rotor blade tip vortex, in *AGARD CP-111*, 13–15 Sept 1972
5. D.W. Boatwright, Measurements of velocity components in the wake of a full-scale helicopter rotor in hover. in *Technical Report USAAMRDL Technical Report 72-33*, U.S. Army Air Mobility Research and Development Laboratory Fort Eustis, Virginia, 1972
6. J.G. Leishman, A.M. Baker, A.J. Coyne, Measurement of rotor tip vortices using three-component LDV. *J. Am. Heli. Soc.* **41**(4), 342 (1995)
7. J.G. Leishman, *Principles of Helicopter Aerodynamics* (Cambridge University Press, Cambridge, 2001)
8. B.G. van der Wall, C.L. Burley, Y.H. Yu, K. Pengel, P. Beaumier, The HART II test—measurement of helicopter rotor wakes. *Aerospace Sci. Tech.* **8**(4), 273–284 (2004)
9. G.E.A. Meier, Computerized background-oriented Schlieren. *Exp. Fluids* **3**, 181 (2002)
10. H. Richard, M. Raffel, Visualization of vortical structures by density gradient detection, in *PSFVIP-3*, Maui, Hawaii, USA, 18–21 June 2001
11. M.J. Hargather, G.S. Settles, Natural-background-oriented Schlieren imaging. *Exp. Fluids* **48**(1), 59 (2009)
12. K. Kindler, E. Goldhahn, F. Leopold, M. Raffel, Recent developments in background oriented Schlieren methods for rotor blade tip vortex measurements. *Exp. Fluids* **43**, 233 (2007)
13. M. Raffel, C. Tung, H. Richard, Y. Yu, G.E.A. Meier, Background oriented stereoscopic schlieren (BOSS) for full scale helicopter vortex characterization, in *9th International Symposium on Flow Visualization*, Edinburgh, UK, 22–25 Aug 2000
14. E. Goldhahn, J. Seume, Background oriented schlieren technique—sensitivity, accuracy, resolution and application to three-dimensional density fields. *Exp. Fluids* **43**, 241 (2007)
15. K.Y. Yick, R. Stocker, T. Peacock, Microscale synthetic Schlieren. *Exp. Fluids* **42**(1), 41 (2007)
16. M. Raffel, C. Willert, S.T. Wereley, J. Kompenhans, *Particle Image Velocimetry—A Practical Guide* (Springer, New York, 2007)
17. M. Raffel, U. Seelhorst, C. Willert, Recording and evaluation methods of PIV investigations on a helicopter rotor model. *Exp. Fluids* **36**, 146 (2004)
18. H. Richard, J. Bosbach, A. Henning, M. Raffel, B.G. van der Wall, 2C and 3C PIV measurements on a rotor in hover condition, in *13th International Symposium on Applications of Laser Techniques to Fluid Mechanics*, Lisbon, Portugal, 26–29 June 2006
19. B.G. van der Wall, H. Richard, Analysis methodology for 3C-PIV data of rotary wing vortices. *Exp. Fluids* **40**, 798 (2006)
20. P.B. Martin, J.G. Pugliese, J.G. Leishman, S.L. Anderson, Stereo PIV measurements in the wake of a hovering rotor, in *56th Annual Forum of the American Helicopter Society*, Virginia Beach, USA, 2–4 May 2000
21. L. Graftieux, M. Michard, N. Grosjean, Combining PIV, POD and vortex identification algorithms for the study of unsteady turbulent swirling flows. *Meas. Sci. Technol.* **12**, 1422 (2001)
22. R. Cucitore, M. Quadrio, A. Baron, On the effectiveness and limitations of local criteria for the identification of a vortex. *Eur. J. Mech. B. Fluids* **18**(2), 261 (1999)

23. K. Kindler, K. Mulleners, H. Richard, B.C. van der Wall, M. Raffel, Aperiodicity in the near-field of full-scale rotor blade tip vortices. *Exp. Fluids* **50**, 10601–1610 (2011)
24. G.H. Vatistas, V. Kozei, W.C. Mih, A simpler model for concentrated vortices. *Exp. Fluids* **11**, 73 (1991)
25. A. Bagai, J.G. Leishman, Flow visualization of compressible vortex structures using density gradient techniques. *Exp. Fluids* **15**, 431 (1993)